Published in final edited form as:
J Struct Biol. 2010 February ; 169(2): 243. doi:10.1016/j.jsb.2009.11.005.

QUATERNARY STRUCTURE OF K_{ATP} CHANNEL SUR2A NUCLEOTIDE BINDING DOMAINS RESOLVED BY SYNCHROTRON RADIATION X-RAY SCATTERING

Sungjo Park and **Andre Terzic***
Marriott Heart Disease Research Program, Division of Cardiovascular Diseases, Departments of Medicine, Molecular Pharmacology and Experimental Therapeutics, and Medical Genetics, Mayo Clinic, Rochester, Minnesota 55905, USA

Abstract

Heterodimeric nucleotide binding domains NBD1/NBD2 distinguish the ATP-binding cassette protein SUR2A, a recognized regulatory subunit of cardiac ATP-sensitive K^+ (K_{ATP}) channels. The tandem function of these core domains ensures metabolism-dependent gating of the Kir6.2 channel pore, yet their structural arrangement has not been resolved. Here, purified monodisperse and interference-free recombinant particles were subjected to synchrotron radiation small-angle X-ray scattering (SAXS) in solution. Intensity function analysis of SAXS profiles resolved NBD1 and NBD2 as octamers. Implemented by *ab initio* simulated annealing, shape determination prioritized an oblong envelope wrapping NBD1 and NBD2 with respective dimensions of 168 × 80 × 37 $Å^3$ and 175 × 81 × 37 $Å^3$ based on symmetry constraints, validated by atomic force microscopy. Docking crystal structure homology models against SAXS data reconstructed the NBD ensemble surrounding an inner cleft suitable for Kir6.2 insertion. Human heart disease-associated mutations introduced *in silico* verified the criticality of the mapped protein-protein interface. The resolved quaternary structure delineates thereby a macromolecular arrangement of K_{ATP} channel SUR2A regulatory domains.

Keywords

ATP-sensitive K^+ channel; Kir6.2; SUR2A; small angle x-ray scattering; mutation; structure

1. Introduction

The ATP-binding cassette (ABC) transporters are evolutionarily conserved transmembrane proteins, with canonical family members characterized by ATP hydrolysis-driven substrate translocation that accounts for diverse biological processes ranging from nutrient import to toxin efflux (Dean, 2005; Linton, 2007; Linton and Higgins, 2007; Rees et al., 2009). Atypical ABC proteins have also been identified, and account for substrate translocation-independent functions, such as ion channel gating (Aittoniemi et al., 2009; Burke et al., 2008; Higgins and

*Corresponding author: A. Terzic, Mayo Clinic, 200 First Street SW, Rochester, MN 55905, USA; Tel: +1 507-284-2747; Fax: +1 507-266-9936; terzic.andre@mayo.edu

Linton, 2004; Moreau et al., 2008). A case in point is the sulfonylurea receptor 2A (SUR2A), a distinctive ABC protein that regulates the operation of the ATP-sensitive potassium (K_{ATP}) channels in cardiac myocytes (Alekseev et al., 2005; Ashcroft, 2006; Inagaki et al., 1996; Inagaki et al., 1995; Nichols, 2006; Wheeler et al., 2008).

Encoded by *ABCC9*, SUR2A belongs to the ABCC subfamily along the cystic fibrosis transmembrane conductance regulator (CFTR or ABCC7) and the multidrug resistance-related protein (MRP or ABCC1) (Biemans-Oldehinkel et al., 2006; Chutkow et al., 1996; Oram and Vaughan, 2006; Solbach et al., 2006; Yamada and Kurachi, 2005). Through physical association with the potassium channel Kir6.2 pore, SUR2A endows K_{ATP} channel complexes with a unique metabolic decoding capacity that assures linkage of the cellular energetic state with membrane excitability (Bryan et al., 2006; Dupuis et al., 2008; Lorenz and Terzic, 1999; Zingman et al., 2007). SUR2A harbors essential nucleotide binding domains - NBD1 and NBD2. Each NBD encompasses Walker A (GX_4GKS/T), Walker B (Φ_4DD/E; Φ represents hydrophobic residues) and linker (LSGGQ) signature motifs (Walker et al., 1982). Responsible for adenine nucleotide recognition and processing, the SUR2A NBD1/2 tandem is integral in transduction of metabolic signals to the K_{ATP} channel pore (Bienengraeber et al., 2000; Karger et al., 2008; Zingman et al., 2001; Zingman et al., 2002). Genetic mutations in SUR2A NBDs alter channel function, and human K_{ATP} channelopathies have been implicated in cardiac disease susceptibility underscoring the structural integrity of regulatory domains in optimal channel performance (Bienengraeber et al., 2004; Kane et al., 2005; Olson et al., 2007; Reyes et al., 2009; Sattiraju et al., 2008).

To date, over 50 crystal structures of isolated NBDs from both bacterial and eukaryotic ABC transporters have been resolved (Hollenstein et al., 2007; Linton and Higgins, 2007; Moussatova et al., 2008; Rees et al., 2009). Despite the wealth of information pertinent to NBD structures of canonical ABC proteins, little is known regarding atypical ABC counterparts, including the mammalian SUR2A NBDs. In part, the lack of information is due to challenges in protein expression and chaotic orientation in solution that impede crystal formation. Although a molecular model of SUR2A NBD dimers has provided an initial discrete domain map (Park et al., 2008), the actual shape underlying structural arrangement remains uncertain.

Small angle X-ray scattering (SAXS) offers an approach to delineate supramolecular conformations (Hura et al., 2009; Petoukhov and Svergun, 2007; Putnam et al., 2007). Here, SAXS, in tandem with *ab initio* and rigid body model reconstruction, was applied to decipher the molecular envelope of SUR2A nucleotide binding domains in solution. We report a quaternary structural portrait of NBD1/NBD2 that provides a blueprint of structural constraints within regulatory K_{ATP} channel domains.

2. Materials and methods

2.1. Purified SUR2A NBD1 and NBD2

Murine cDNA SUR2A (GenBank D86037; kindly provided by Dr. S. Seino) encoding NBD1 (D666-890) and NBD2 (G1301-K1546) were amplified by PCR, and incorporated into a modified pET-15b vector (Novagen) containing the N-terminal $(His)_6$-tag and TEV protease cleavage site. Plasmids were transformed in the *E. coli* Rosetta(DE3)pLysS strain (Novagen), and NBD1 as well as NBD2 proteins purified (Park et al., 2008). Pelleted cells were suspended in buffer A (50 mmol/L Tris-HCl, 50 mmol/L NaCl, 1 mmol/L TCEP, 0.5 mmol/L EDTA and 5% glycerol (pH 8.0)), lyzed with a high-pressure microfluidizer Emulsiflex C-5 (Avestin), incubated for 20 min after mixing with 1% Triton X-100, and centrifuged at 20,000*g* for 30 min. Pellets were resuspended in buffer A containing 1% Triton X-100, homogenized, and centrifuged at 9,000*g* for 20 min. These steps were repeated three times. Residual Triton X-100 was removed in buffer A followed by repeated centrifugation at 9,000*g* for 20 min. Washed

pellets were resuspended in denaturation buffer (50 mmol/L Tris-HCl, 50 mmol/L NaCl, 5 mmol/L TCEP, 0.5 mmol/L EDTA, and 5% glycerol (pH 8.0)), and incubated with 4.5% N-lauroylsarcosine for 30 min. Solutions were passed through a 0.45 μm filter to exclude aggregates, and dialyzed at least three times against 2 L of 10 mmol/L Tris-HCl (pH 8.0), 0.05 mmol/L EDTA, 0.1 mmol/L TCEP and 0.03% N-lauroylsarcosine, used below the critical micelle concentration (Frankel et al., 1991). Refolded NBDs were subject to gel filtration using a Superdex 200 column (Amersham Biosciences) with 10 mmol/L Tris, 0.05 mmol/L EDTA, 0.1 mmol/L TCEP and 0.03% N-lauroylsarcosine (pH 8.0). The protein concentration was quantified using an extinction coefficient of 34,045 $(mol/L)^{-1}cm^{-1}$ and 15,845 $(mol/L)^{-1}cm^{-1}$ for NBD1 and NBD2 respectively, and the purity was determined by densitometry.

2.2. Circular Dichroism Spectroscopy

The far-UV and near-UV circular dichroism (CD) spectra of refolded NBDs were recorded within the 250 to 200 nm and 325 to 250 nm range, respectively, on a JASCO J715 CD spectropolarimeter (Park et al., 2008). The mean residue ellipticity ([θ] in deg cm^2 $dmol^{-1}$) was calculated as (mdeg x MRW)/(10*lc*), where mdeg is the observed ellipticity in millidegrees; MRW, the mean residue weight; *l*, the optical path in cm; and c, the concentration in mg/ml. Based on UV circular dichroism, the secondary structure of NBDs was analyzed using neural network algorithms (http://geneura.ugr.es/cgi-bin/somcd/index.cgi), while the characteristics defining tertiary structure were evaluated against random coil denatured protein profile (Unneberg et al., 2001).

2.3. ATPase Activity

The ATPase activity of purified NBDs was measured based on inorganic phosphate production detected by colorimetry (Park et al., 2008). Assays were performed in 10 mmol/L Tris, 0.2 mmol/L TCEP, 10 mmol/L $MgCl_2$, 0.03% N-lauroylsarcosine and 4 mmol/L ATP (pH 8) at 37°C. The produced inorganic phosphate absorption was measured at 850 nm.

2.4. Synchrotron Radiation Small Angle X-ray Scattering

Synchrotron radiation small angle X-ray scattering (SAXS) profiles were collected using the SIBYLS beamline 12.3.1 at the Advance Light Source (ALS) at Lawrence Berkeley National Laboratories (Hura et al., 2009). A wavelength of 1.0332 Å was applied with a sample to detector distance of 1.5 m, which resulted in the scattering vector, *q*, ranging from 0.01 to 0.32 $Å^{-1}$. The scattering intensity, *I(q)*, was recorded as a function of the scattering vector, defined as $q = 4\pi\sin\theta/\lambda$, where 2θ is the angle between the incident and scattered radiation and λ is the wavelength of the incident X-ray beam. Measurements were carried at 10°C. Samples of NBD1 and NBD2 proteins were prepared in the concentration range of 1.5 to 11.4 mg/ml in 10 mmol/L Tris (pH 8), 1 mmol/L TCEP, 0.05 mmol/L EDTA, 0.03% N-lauroylsarcosine and 5% glycerol. Scattering data from buffer (background) *versus* protein (sample at different concentrations) were collected alternately in the short (6 s), long (60 s), and short (6 s) exposure sequence. Short exposure readouts were compared to ensure that no radiation-induced protein damage had occurred, and data were merged using the PRIMUS program (Svergun and Koch, 2002). In a limited set of experiments, SAXS measurements pertinent to initial reference samples were conducted under similar experimental conditions using the beamline DND-CAT (5IDD) at the Advanced Photon Source (APS), Argonne National Laboratory.

2.5. Data Evaluation and Analysis

The radius of gyration (R_G) was derived by the Guinier approximation using the low *q*-regions of scattering profiles, $I(q) = I(0) \exp(-q^2R_G^2/3)$ for $qR_G < 1.3$, which extrapolated scattering intensity to the zero angle, *I(0)*. The radius of gyration (R_G) and the intensity measured at zero angle (*I(0)*), extracted from the Guinier plot, displayed limited NBD1 or NBD2 concentration-

dependence (Supplementary Fig. 1A) indicating lack of interparticle interference and validating monodispersity, prerequisites for SAXS analysis (Petoukhov and Svergun, 2007; Putnam et al., 2007; Svergun and Koch, 2002). In response to escalating NBD1 or NBD2 concentrations, the forward scattering intensity was proven linear (Supplementary Fig. 1B), verifying absence of aggregation and maintenance of NBDs in a refolded state (Putnam et al., 2007; Putnam et al., 2001). The distance distribution function, *P(r)*, representing the probability of finding a point within the observed particle at a distance, *r*, from a defined point of reference, was calculated using the indirect Fourier transform method implemented in the bioinformatics package GNOM (Svergun, 1992). This analysis provided values of R_G and *I(0)* based on the entire SAXS data set, and compared favorably to values derived from Guinier plots. To determine maximum protein dimensions (D_{max}), the *P(r)* function was computed while constraining the function to zero at r_{max}, where r_{max} varied from 130 to 220 Å in 5 Å increments and the r_{max} yielded a plausible *P(r)* defined D_{max}.

2.6. Atomic Force Microscopy

Atomic force microscopy applied in contact mode was performed using the Nanoscope IV PicoForce Multimode AFM equipped with an E-scanner and V shaped silicon nitride cantilevers with a 0.06 N/m spring constant (Veeco Instruments) (Park et al., 2008). NBDs (2–40 μg/ml) were placed on freshly cleaved mica discs, and dried with nitrogen gas. After 30 min, unbound proteins and buffers were washed from the mica surface with water, and NBD-absorbed mica dried again. Data were collected in both height and phase modes. Images (512×512 pixels) were analyzed using the Nanoscope Version 6.13 software.

2.7. Ab initio Reconstruction

The molecular outlines of NBD1 and NBD2 were constructed from experimental SAXS data using the *ab initio* stimulated annealing programs DAMMIN and GASBOR (Svergun, 1999; Svergun et al., 2001). By minimizing the discrepancy (χ^2) between calculated and experimental SAXS data, these programs search a chain-compatible spatial distribution of beads or dummy residues centered on the C_α atoms of the protein:

$$\chi^2=\frac{1}{N-1}\sum_i\left[\frac{I(q_i)_{\text{exp.}}-cI(q_i)_{\text{calc.}}}{\sigma(q_i)}\right]^2$$

where N is the number of experimental points; c, the scaling factor; $I(q_i)_{exp.}$ and $I(q_i)_{calc.}$, the experimental and calculated intensity, respectively; and $\sigma(q_i)$, the experimental error at the momentum transfer q_i. In order to identify a most probable model, multiple independent runs were required to decrease the risk of over interpretation of underdetermined models (Putnam et al., 2007). Specifically, sixteen independent runs for each NBD were performed using a set of symmetries to generate a series of plausible reconstructions. Reflective of octameric permutations, P1, P2, P4, P8 and P222 were selected to optimize *ab initio* reconstruction. P1 reflects no symmetry, P2 corresponds to one 2-fold symmetry, P4 to one 4-fold symmetry, P8 to one 8-fold symmetry, and P222 to three perpendicular 2-folds symmetry. Under these symmetry conditions, the χ^2 values ranged from 0.703 to 0.747 for NBD1, and from 0.633 to 0.701 for NBD2. Using the program package DAMAVER/DAMFILT (Volkov and Svergun, 2003), reconstructed models were aligned, averaged, and scored with a normalized spatial discrepancy (NSD) parameter that characterizes conversions among *ab initio* structures. Models with a large NSD (> mean NSD + 2 χ variation of NSD) were discarded.

2.8. Model Building

As no crystallographic structure of SUR2A NBD1 or NBD2 currently exists, homology models of NBDs were built. To this end, NBDs sequences from SUR2A were aligned using ClustalX with hemolysin B (HylB) that shares 29% sequence identity. Three-dimensional models of homodimer NBD1, NBD2, or heterodimer NBD1/NBD2 were generated using the homology modeling program MODELLER 6 based on the 2.5 Å crystal structure of the HylB-NBD dimer template (PBD: 1XEF) (Park et al., 2008). Purified recombinant NBDs had 23 N-terminal pre-residues randomly oriented in solution, accounting for 20 conformations resolved by NMR (PDB: 2HFV). Distinct conformations were added to the N-terminus of the NBD homology models. Rigid body modeling of the NBD quaternary structure was performed in the q range of 0.01–0.22 $Å^{-1}$. The scattering amplitudes of homology models were calculated using the CRYSOL program, which predict a theoretical SAXS pattern with given atomic coordinates (Svergun et al., 1995). The quaternary structure was generated by GLOBSYMM, a brute-force modeling program (Petoukhov and Svergun, 2005), using exhaustive searches to screen for the best fit produced by rigid body movements and rotations of the crystallographic NBD dimer under P222 symmetry without steric clashes. Primary contacts between subunits within the resolved quaternary ensemble were delineated by randomly oriented N-terminal pre-residues, deleted from final models for clarity.

3. Results

3.1. Secondary and Tertiary Structures from Purified SUR2A NBDs

The nucleotide binding domains, NBD1 and NBD2, of the K_{ATP} channel *ABCC9*-encoded SUR2A were individually expressed in *E. coli*, refolded and purified by gel filtration chromatography. Recombinant proteins, with purity >92%, migrated at corresponding molecular weights on SDS-PAGE (Fig. 1A), and formed oligomers detected on size-exclusion chromatography (Fig. 1B). Purified NBDs displayed a distinctive secondary structure in far-UV circular dichroism spectroscopy reflecting peptide backbone transitions with profiles composed of 66% α-helix, 9% β-sheet, 7% turn and 18% random coil for NBD1, and 40% α-helix, 20% β-sheet, 11% turn and 29% random coil for NBD2 (Fig. 1C). In near-UV circular dichroism spectroscopy, where tertiary conformation is attributed to aromatic amino acids or disulfide bond interactions, purified NBD1 and NBD2 demonstrated a well-folded structure (Fig. 1D) with detectable ATPase activity (Fig. 1D inset), indicating intrinsic structural and functional integrity.

3.2. Synchrotron Radiation X-Ray Scattering Profiles of NBD1 and NBD2

Synchrotron radiated NBD1 and NBD2 molecules displayed an intensity (I) *versus* scattering vector (q) profile (Fig. 2A) with linear dependence, solved by the Guinier function, i.e., $\log(I(q))$ *versus* $(q)^2$, that demonstrated monodispersity (Fig. 2A inset), distinguishable from aggregated samples indicated by non-linear dependence (Putnam et al., 2007). Synchrotron radiation-based quality control established a profile of recombinant NBD1 and NBD2 proteins amenable for structural deconvolution (Supplementary Fig. 1A and 1B). The distance distribution function $P(r)$, which represents the probable distribution of interatomic distances, was implemented through indirect Fourier transformation (Svergun, 1992), and displayed a radius of gyration (R_G) and a maximum molecular dimension (D_{max}) of 55.3±0.2 Å and 170 ±8 Å for NBD1 (n=5), and 59.3±0.3 Å and 180±12 Å for NBD2 (n=5), respectively (Fig. 2B). The size of NBDs was independently validated by atomic force microscopy at nanoscale resolution (n=8; Fig. 2C). NBD1 and NBD2 particles corresponded to eight assembled monomers extrapolated from the normalized SAXS intensity function (q=0, $I(0)/conc$) (Mylonas and Svergun, 2007;Putnam et al., 2007) through comparison with protein standards (Supplementary Fig. 1C). Thus, SAXS resolved interference-free NBD1 and NBD2 proteins as octameric architectures with maximum dimensions of 170 and 180 Å, respectively.

3.3. Ab initio Reconstruction of NBD Envelope

The macromolecular fit for NBD1 or NBD2 proteins was constructed by imposing symmetry constraints using *ab initio* simulated annealing (Svergun, 1999). To attain optimal symmetry, five different conditions (P1, P2, P4, P8 and P222) reflective of octameric permutations were assessed (Putnam et al., 2007). Initial computation, launched with a chain-compatible spatial distribution of beads (Volkov and Svergun, 2003), built a spectrum of macromolecular shapes. Sixteen independent runs per each symmetry condition were aligned, averaged, and scored with the normalized spatial discrepancy (NSD) index to prioritize the best constraint while minimizing discrepancies (χ^2) between calculated and experimental SAXS outputs (Fig. 3A). Average χ^2 values from NBD1 *ab initio* reconstructions were 0.7340±0.0009 for P1, 0.7370 ±0.0006 for P2, 0.7337±0.0011 for P4, 0.7238±0.0027 for P8 and 0.7340±0.0007 for P222 (n=16; Fig. 3A). In addition, mean values of normalized spatial discrepancy (NSD) of NBD1 were 0.575 for P1, 1.195 for P2, 0.766 for P4, 1.090 for P8, and 0.687 for P222 (n=16; Fig. 3A). Although simulations produced under P8 symmetry exhibited the lowest χ^2 value, the NSD under P8 demonstrated a wide variation similar to P2. Envelopes constructed under P4 symmetry or without symmetry restraint (P1) provided less variation than P8 or P2 models. Imposing the highest symmetry (P222) produced the most convergent model with the lowest discrepancy between calculated and experimental data (Fig. 3A). Indeed, residual curves imposed by P222 symmetry obtained from the fit to the desmeared and smoothed data from GNOM showed lower variation compared to the P8 symmetry constrain (Supplementary Fig. 2). The P222-based *ab initio* NBD1 model disclosed an oblong shape with composite dimensions of 168 × 80 × 37 $Å^3$ (Fig. 3B and Fig. 3C). Similarly, *ab initio* modeling of NBD2 under different symmetry conditions was evaluated. Average χ^2 values from NBD2 reconstructions were 0.6767±0.0013 for P1, 0.6768±0.0011 for P2, 0.6841±0.0017 for P4, 0.6640±0.0046 for P8 and 0.6794±0.0022 for P222 (n=16; Fig. 3D). The mean values of NSD were 0.621 for P1, 1.059 for P2, 0.678 for P4, 1.497 for P8, and 0.789 for P222 (n=16; Fig. 3D). An imposed P222 symmetry retained an optimized χ^2 agreement and NSD values, revealing an oblong shape with averaged dimensions of 175 × 81 × 37 $Å^3$ (Fig. 3E and Fig. 3F). Reconstruction was independently verified through a progressive spatial distribution run of dummy residues centered on the C_α atoms of the protein (Supplementary Fig. 3). Thus, *ab initio* reconstruction divulged oblong envelopes holding NBD1 and NBD2 proteins.

3.4. Quaternary NBDs Structures Resolved by Rigid Body Modeling

By docking crystal structure homology models (Putnam et al., 2007) against experimentally defined SAXS data, the quaternary structures of NBD1 (Fig. 4A) and NBD2 (Fig. 4B) were mapped onto SAXS envelopes. Based on P222 symmetry constraints, NBDs were resolved as tetrameric dimers that fulfilled the SAXS deduced octameric arrangement. Starting from a stochastically positioned crystallographic homodimer under P222 symmetry, atomic coordinates for NBD1 or NBD2 were computed using the CRYSOL platform (Svergun et al., 1995) to predict X-ray scattering amplitude patterns. Iterations with the modeling program GLOBSYMM (Petoukhov and Svergun, 2005) revealed a homodimeric quaternary structure for NBD1 (Fig. 4A) and NBD2 (Fig. 4B). From independent program runs with different Fibonacci grid orders, the best reconstructed model fitted experimental data with χ^2=2.69 for NBD1 and χ^2=4.09 for NBD2. It should be noted that a homology model used to fit the low resolution SAXS profile, as well as randomly oriented N-terminal pre-residues, could impact fitting (Putnam et al., 2007). The reconstructed models under P222 symmetry had a significantly better correlation with SAXS data than other symmetry models (e.g., for P4 symmetry see Supplementary Fig. 4). As the root mean square deviation between homodimer NBD1 or NBD2 and heterodimer NBD1/NBD2 was 0.54 Å or 0.58 Å, respectively, i.e., values <1 Å, the quaternary structure of the NBD1/NBD2 heterodimer was derived from homomeric NBD1 and NBD2 SAXS profiles. Although this approach is abstract, in the predicted model of heterodimeric NBD1/NBD2 quaternary structure (χ^2=2.86), NBD2 was consistently

oriented at the outside of the octameric ring while NBD1 was positioned at the inside of the octameric ring facing a central opening with a diameter of ~35 Å (Fig. 4C). Such opening could incorporate a macromolecular structure with dimensions equivalent to the Kir6.2 channel pore (Mikhailov et al., 2005) reconstructing a K_{ATP} channel complex.

3.5. Structural Consequences of Pathogenic SUR2A NBD1/NBD2 Mutations

Susceptibility to human heart disease has been linked to genetic defects in *ABCC9*-encoded SUR2A (Bienengraeber et al., 2004; Minoretti et al., 2006; Olson et al., 2007). This includes the NBD1 V734I variant (Fig. 5A), associated with myocardial infarction, and the NBD2 A1513T and T1547I mutations implicated in dilated cardiomyopathy and stress-induced atrial fibrillation, respectively (Fig. 5B). Here, the resolved structures based on low resolution SAXS data guided a targeted evaluation of human heart disease-associated mutations. The A1513 mutation, replaced with a bulky nucleophilic T residue, mapped in the NBD2 monomer to the C-terminal β-strand in close proximity with the Walker A motif, and disrupted the tertiary protein structure leading to disarray of this function-critical region (Fig. 5B). While the monomeric structure could not decisively address the structural consequences of either V734I or T1547I mutations due to their remote positions from critical functional motifs (Fig. 5A and 5B), resolved heterodimer and quaternary structures were able to trace anticipated structural implications. Specifically, the NBD2 T1547I, whereby a nucleophilic residue is substituted with a somewhat larger hydrophobic residue found at the tail of the isoform-specific SUR2A C-terminal α-helix (Fig. 5B), compromised solvent accessibility due to proximity from the NBD1/NBD2 heterodimer interface (Fig. 5C). Though the NBD1 V734 mutation swapped with a larger I residue was charted at a loop region distant to either Walker A or Walker B motifs (Fig. 5A), the resolved quaternary structure indicated that the afflicted residue was at the juncture between regulatory NBD1/NBD2 domains and the groove for channel protein insertion (Fig. 5D). Pathogenic mutations are thereby demonstrated to cluster at locales critical for protein-protein interaction underlying the structural integrity of the K_{ATP} channel complex.

4. Discussion

The atypical ABC protein SUR2A serves as a regulatory subunit of heteromultimeric ATP-sensitive K^+ (K_{ATP}) channels in heart muscle, in particular within the ventricle (Du et al., 2006; Flagg et al., 2008; Inagaki et al., 1996; Li et al., 2000; Nichols, 2006; Shi et al., 2005). Coupling of the pore-forming Kir6.2 with cellular energetic signaling systems relies on cooperative interaction of the SUR2A nucleotide binding domains, NBD1 and NBD2, endowing high-fidelity metabolic sensing properties to the channel complex (Abraham et al., 2002; Alekseev et al., 2005; Zingman et al., 2001; Zingman et al., 2002). While the function of NBD1/NBD2 has been linked to the homeostatic cardioprotective role afforded by K_{ATP} channels (Arrell et al., 2009; Hodgson et al., 2003; Kane et al., 2005; Nichols, 2006; Zingman et al., 2007; Zlatkovic et al., 2009), here synchrotron radiation X-ray scattering was used to resolve the quaternary architecture of these unique nucleotide binding domains. The delineated macromolecular arrangement outlines structural constraints for inter-molecular communication within regulatory domains of the K_{ATP} channel.

Small angle X-ray scattering (SAXS) provided an approach to reveal nanometer-scale structural information and domain organization without the requirement for a crystalline sample. SAXS is particularly valuable to study biomacromolecules within a native solution environment (Hura et al., 2009; Petoukhov and Svergun, 2007; Putnam et al., 2007), and although successful in resolving voltage gated channel domains (Pioletti et al., 2006) or typical ATPases (Davies et al., 2005), atypical ABC proteins - such as the K_{ATP} channel subunit SUR2A - have not been characterized in this manner. Subjected here to synchrotron radiation in solution, the refolded and purified SUR2A NBD1 and NBD2 proteins fulfilled quality

control criteria necessary for structural deconvolution (Putnam et al., 2007). Obtained SAXS profiles mapped an octameric appearance for both NBD1 and NBD2, with the resolved shape and size verified by atomic force microscopy-based nanoimaging.

The presented quaternary ensemble profile based on low resolution SAXS data provides direct structural evidence, at the level of nucleotide binding domain molecules, for the proposed K_{ATP} channel subunit stoichiometry previously limited to anticipated patterns of SUR/Kir6.2 biogenesis and assembly (Clement et al., 1997; Inagaki et al., 1997; Shyng and Nichols, 1997). Captured on electron micrographs, NBD oligomers correspond to a set of eight to nine monomers (de Wet et al., 2007) consistent with the present SAXS readout. *Ab initio* computation here further prioritized candidate oblong envelopes holding NBD1/NBD2 paired octameric ensembles. Structure modeling into constraints of the collected SAXS envelopes provided a refined arrangement that delineated preferential alignment for NBD1 and NBD2 facing toward the inside and outside of the octameric ring, respectively. This organization provides a structural substrate for the functional asymmetry reported for SUR2A NBD1 *versus* NBD2, unique among ABC proteins (Alekseev et al., 2005; Park et al., 2008). Indeed, cooperative NBD1/NBD2 heterodomain interaction, imposed by architectural subunit constraints, ensures intrinsic catalytic activity with vitality for optimal K_{ATP} channel gating (Park et al., 2008; Zingman et al., 2002).

Rigid body modeling of dimer NBDs against SAXS profiles unmasked an inner cleft, amenable for insertion of the Kir6.2 pore. Single-particle electron microscopy measurements have previously suggested that NBDs point towards the central channel pore with a significant tilt away from transmembrane domains (Mikhailov et al., 2005). Such structural implication is in line with independent electron micrography of annular NBDs formations surrounding a void delineated by channel subunit dimensions (de Wet et al., 2007) equivalent to those resolved herein. The putative plane of SUR2A NBDs and channel pore interaction remains at present speculative, and could range along the height of the cytoplasmic Kir6.2 region. Notwithstanding, the spatial arrangement of SUR2A NBD1/NBD2, mapped by SAXS rigid body refinement, indicated that one NBD, namely NBD1, is primarily facing the Kir6.2 channel pore consistent with non-equivalent roles of nucleotide binding domains (Mikhailov et al., 2002). Although speculative, it is noteworthy that based on other ABC proteins a cross-over in the arrangement of SUR NBDs and transmembrane domains (TMDs) (Procko et al., 2009; Rees et al., 2009) could bring a second set of transmembrane domains (TM12-TM17) into proximity to the transmembrane domain of Kir6.2. In fact, about 60 residues located between transmembrane domain 17 and NBD2 have been proposed to physically interact with Kir6.2 (Chan et al., 2003; Dupuis et al., 2008; Rainbow et al., 2004).

Such privileged relationship, in turn, provides a structural rationale for dysregulated channel subunit interaction in the setting of human disease-causing genetic mutations. A case in point is the recently reported variant V734I, implicated in increased susceptibility towards myocardial infarction (Minoretti et al., 2006). The resolved functional quaternary structure of NBDs revealed propinquity between V734 and the delineated inner cleft, a site potentially strategic in channel subunit interaction. More broadly, pathogenic mutations were found to cluster at locales critical for the protein-protein interphase (Ashcroft, 2005; Campbell et al., 2003; Masia and Nichols, 2008; Nichols, 2006) underlying an inherent vulnerability of the K_{ATP} channel complex structure susceptible to genetic variance. Thus, collectively these findings provide an initial structural rationale underlying dysregulation of channel subunit interaction in the setting of human heart disease.

In summary, synchrotron radiation small angle X-ray scattering resolved for the first time the macromolecular arrangement of nucleotide binding domains of *ABCC9*-encoded SUR2A. The delineated quaternary structure, based on low resolution SAXS data, revealed architectural

constraints within the charted molecular envelope wrapping NBD1/NBD2 octamers, with dimensions validated by atomic force microscopy. The asymmetric domain alignment within the rigid body ensemble unmasked a structural substrate vulnerable to disease-provoked distortion. Deconvoluted NBD1 and NBD2 heterodomains establish, thereby, a structural map of critical K_{ATP} channel regulatory domains potentially useful in anticipating the consequences imposed by genetic variations among individuals.

Supplementary Material

Refer to Web version on PubMed Central for supplementary material.

Acknowledgments

We thank the SIBYLS beamline 12.3.1 staff at the Advance Light Source (ALS) at Lawrence Berkeley National Laboratories for assistance with synchrotron data collection. We acknowledge the organizers of SXS2008 at the Advanced Photon Source (APS) for support with experiments at beamline DND-CAT. Authors express their gratitude to Drs. Georges Mer and Christina Miranda D. Correia (Mayo Clinic) for expert discussions. This work was supported by the NIH (R01 HL064822), and Marriott Heart Disease Research Program.

REFERENCES

Abraham MR, Selivanov VA, Hodgson DM, Pucar D, Zingman LV, Wieringa B, Dzeja PP, Alekseev AE, Terzic A. Coupling of cell energetics with membrane metabolic sensing. Integrative signaling through creatine kinase phosphotransfer disrupted by M-CK gene knock-out. J Biol Chem 2002;277:24427–34. [PubMed: 11967264]

Aittoniemi J, Fotinou C, Craig TJ, de Wet H, Proks P, Ashcroft FM. SUR1: A unique ATP-binding cassette protein that functions as an ion channel regulator. Philos Trans R Soc Lond B Biol Sci 2009;364:257–67. [PubMed: 18990670]

Alekseev AE, Hodgson DM, Karger AB, Park S, Zingman LV, Terzic A. ATP-sensitive K^+ channel channel/enzyme multimer: metabolic gating in the heart. J Mol Cell Cardiol 2005;38:895–905. [PubMed: 15910874]

Arrell DK, Zlatkovic J, Kane GC, Yamada S, Terzic A. ATP-sensitive K^+ channel knockout induces cardiac proteome remodeling predictive of heart disease susceptibility. J Proteome Res 2009;8:4823–34. [PubMed: 19673485]

Ashcroft FM. ATP-sensitive potassium channelopathies: focus on insulin secretion. J Clin Invest 2005;115:2047–58. [PubMed: 16075046]

Ashcroft FM. From molecule to malady. Nature 2006;440:440–7. [PubMed: 16554803]

Biemans-Oldehinkel E, Doeven MK, Poolman B. ABC transporter architecture and regulatory roles of accessory domains. FEBS Lett 2006;580:1023–35. [PubMed: 16375896]

Bienengraeber M, Alekseev AE, Abraham MR, Carrasco AJ, Moreau C, Vivaudou M, Dzeja PP, Terzic A. ATPase activity of the sulfonylurea receptor: a catalytic function for the K_{ATP} channel complex. FASEB J 2000;14:1943–52. [PubMed: 11023978]

Bienengraeber M, Olson TM, Selivanov VA, Kathmann EC, O'Cochlain F, Gao F, Karger AB, Ballew JD, Hodgson DM, Zingman LV, Pang YP, Alekseev AE, Terzic A. *ABCC9* mutations identified in human dilated cardiomyopathy disrupt catalytic K_{ATP} channel gating. Nat Genet 2004;36:382–7. [PubMed: 15034580]

Bryan J, Munoz A, Zhang X, Dufer M, Drews G, Krippeit-Drews P, Aguilar-Bryan L. ABCC8 and ABCC9: ABC transporters that regulate K^+ channels. Pflugers Arch 2006;453:703–18. [PubMed: 16897043]

Burke MA, Mutharasan RK, Ardehali H. The sulfonylurea receptor, an atypical ATP-binding cassette protein, and its regulation of the K_{ATP} channel. Circ Res 2008;102:164–76. [PubMed: 18239147]

Campbell JD, Sansom MS, Ashcroft FM. Potassium channel regulation. EMBO Rep 2003;4:1038–42. [PubMed: 14593442]

Chan KW, Zhang H, Logothetis DE. N-terminal transmembrane domain of the SUR controls trafficking and gating of Kir6 channel subunits. EMBO J 2003;22:3833–43. [PubMed: 12881418]

Chutkow WA, Simon MC, Le Beau MM, Burant CF. Cloning, tissue expression, and chromosomal localization of SUR2, the putative drug-binding subunit of cardiac, skeletal muscle, and vascular K_{ATP} channels. Diabetes 1996;45:1439–45. [PubMed: 8826984]

Clement JP, Kunjilwar K, Gonzalez G, Schwanstecher M, Panten U, Aguilar-Bryan L, Bryan J. Association and stoichiometry of K_{ATP} channel subunits. Neuron 1997;18:827–38. [PubMed: 9182806]

Davies JM, Tsuruta H, May AP, Weis WI. Conformational changes of p97 during nucleotide hydrolysis determined by small-angle X-ray scattering. Structure 2005;13:183–95. [PubMed: 15698563]

de Wet H, Mikhailov MV, Fotinou C, Dreger M, Craig TJ, Venien-Bryan C, Ashcroft FM. Studies of the ATPase activity of the ABC protein SUR1. FEBS J 2007;274:3532–44. [PubMed: 17561960]

Dean M. The genetics of ATP-binding cassette transporters. Methods Enzymol 2005;400:409–29. [PubMed: 16399363]

Du Q, Jovanovic S, Clelland A, Sukhodub A, Budas G, Phelan K, Murray-Tait V, Malone L, Jovanovic A. Overexpression of SUR2A generates a cardiac phenotype resistant to ischemia. FASEB J 2006;20:1131–41. [PubMed: 16770012]

Dupuis JP, Revilloud J, Moreau CJ, Vivaudou M. Three C-terminal residues from the sulphonylurea receptor contribute to the functional coupling between the K_{ATP} channel subunits SUR2A and Kir6.2. J Physiol 2008;586:3075–85. [PubMed: 18450778]

Flagg TP, Kurata HT, Masia R, Caputa G, Magnuson MA, Lefer DJ, Coetzee WA, Nichols CG. Differential structure of atrial and ventricular K_{ATP}: atrial K_{ATP} channels require SUR1. Circ Res 2008;103:1458–65. [PubMed: 18974387]

Frankel S, Sohn R, Leinwand L. The use of sarkosyl in generating soluble protein after bacterial expression. Proc Natl Acad Sci U S A 1991;88:1192–6. [PubMed: 1705029]

Higgins CF, Linton KJ. The ATP switch model for ABC transporters. Nat Struct Mol Biol 2004;11:918–26. [PubMed: 15452563]

Hodgson DM, Zingman LV, Kane GC, Perez-Terzic C, Bienengraeber M, Ozcan C, Gumina RJ, Pucar D, O'Coclain F, Mann DL, Alekseev AE, Terzic A. Cellular remodeling in heart failure disrupts K_{ATP} channel-dependent stress tolerance. EMBO J 2003;22:1732–42. [PubMed: 12682006]

Hollenstein K, Dawson RJ, Locher KP. Structure and mechanism of ABC transporter proteins. Curr Opin Struct Biol 2007;17:412–8. [PubMed: 17723295]

Hura GL, Menon AL, Hammel M, Rambo RP, Poole FL 2nd, Tsutakawa SE, Jenney FE Jr. Classen S, Frankel KA, Hopkins RC, Yang SJ, Scott JW, Dillard BD, Adams MW, Tainer JA. Robust, high-throughput solution structural analyses by small angle X-ray scattering (SAXS). Nat Methods 2009;6:606–12. [PubMed: 19620974]

Inagaki N, Gonoi T, Seino S. Subunit stoichiometry of the pancreatic beta-cell ATP-sensitive K^+ channel. FEBS Lett 1997;409:232–6. [PubMed: 9202152]

Inagaki N, Gonoi T, Clement JP, Wang CZ, Aguilar-Bryan L, Bryan J, Seino S. A family of sulfonylurea receptors determines the pharmacological properties of ATP-sensitive K^+ channels. Neuron 1996;16:1011–7. [PubMed: 8630239]

Inagaki N, Gonoi T, Clement JP, Namba N, Inazawa J, Gonzalez G, Aguilar-Bryan L, Seino S, Bryan J. Reconstitution of IK_{ATP}: an inward rectifier subunit plus the sulfonylurea receptor. Science 1995;270:1166–70. [PubMed: 7502040]

Kane GC, Liu XK, Yamada S, Olson TM, Terzic A. Cardiac K_{ATP} channels in health and disease. J Mol Cell Cardiol 2005;38:937–43. [PubMed: 15910878]

Karger AB, Park S, Reyes S, Bienengraeber M, Dyer RB, Terzic A, Alekseev AE. Role for SUR2A ED domain in allosteric coupling within the K_{ATP} channel complex. J Gen Physiol 2008;131:185–96. [PubMed: 18299394]

Li RA, Leppo M, Miki T, Seino S, Marban E. Molecular basis of electrocardiographic ST-segment elevation. Circ Res 2000;87:837–9. [PubMed: 11073877]

Linton KJ. Structure and function of ABC transporters. Physiology (Bethesda) 2007;22:122–30. [PubMed: 17420303]

Linton KJ, Higgins CF. Structure and function of ABC transporters: the ATP switch provides flexible control. Pflugers Arch 2007;453:555–67. [PubMed: 16937116]

Lorenz E, Terzic A. Physical association between recombinant cardiac ATP-sensitive K^+ channel subunits Kir6.2 and SUR2A. J Mol Cell Cardiol 1999;31:425–34. [PubMed: 10093054]

Masia R, Nichols CG. Functional clustering of mutations in the dimer interface of the nucleotide binding folds of the sulfonylurea receptor. J Biol Chem 2008;283:30322–9. [PubMed: 18715873]

Mikhailov MV, Mikhailova EA, Ashcroft SJ. Structure-function relationships in the beta-cell K_{ATP} channel. Biochem Soc Trans 2002;30:323–7. [PubMed: 12023873]

Mikhailov MV, Campbell JD, de Wet H, Shimomura K, Zadek B, Collins RF, Sansom MS, Ford RC, Ashcroft FM. 3-D structural and functional characterization of the purified K_{ATP} channel complex Kir6.2-SUR1. EMBO J 2005;24:4166–75. [PubMed: 16308567]

Minoretti P, Falcone C, Aldeghi A, Olivieri V, Mori F, Emanuele E, Calcagnino M, Geroldi D. A novel Val734Ile variant in the *ABCC9* gene associated with myocardial infarction. Clin Chim Acta 2006;370:124–8. [PubMed: 16563363]

Moreau CJ, Dupuis JP, Revilloud J, Arumugam K, Vivaudou M. Coupling ion channels to receptors for biomolecule sensing. Nat Nanotechnol 2008;3:620–5. [PubMed: 18839002]

Moussatova A, Kandt C, O'Mara ML, Tieleman DP. ATP-binding cassette transporters in *Escherichia coli*. Biochim Biophys Acta 2008;1778:1757–1771. [PubMed: 18634750]

Mylonas F, Svergun DI. Accuracy of molecular mass determination of proteins in solution by small-angle X-ray scattering. J Appl Cryst 2007;40(Suppl):s245–s249.

Nichols CG. K_{ATP} channels as molecular sensors of cellular metabolism. Nature 2006;440:470–6. [PubMed: 16554807]

Olson TM, Alekseev AE, Moreau C, Liu XK, Zingman LV, Miki T, Seino S, Asirvatham SJ, Jahangir A, Terzic A. K_{ATP} channel mutation confers risk for vein of Marshall adrenergic atrial fibrillation. Nat Clin Pract Cardiovasc Med 2007;4:110–6. [PubMed: 17245405]

Oram JF, Vaughan AM. ATP-binding cassette cholesterol transporters and cardiovascular disease. Circ Res 2006;99:1031–43. [PubMed: 17095732]

Park S, Lim BB, Perez-Terzic C, Mer G, Terzic A. Interaction of asymmetric *ABCC9*-encoded nucleotide binding domains determines K_{ATP} channel SUR2A catalytic activity. J Proteome Res 2008;7:1721–8. [PubMed: 18311911]

Petoukhov MV, Svergun DI. Global rigid body modeling of macromolecular complexes against small-angle scattering data. Biophys J 2005;89:1237–50. [PubMed: 15923225]

Petoukhov MV, Svergun DI. Analysis of X-ray and neutron scattering from biomacromolecular solutions. Curr Opin Struct Biol 2007;17:562–71. [PubMed: 17714935]

Pioletti M, Findeisen F, Hura GL, Minor DL Jr. Three-dimensional structure of the KChIP1-Kv4.3 T1 complex reveals a cross-shaped octamer. Nat Struct Mol Biol 2006;13:987–95. [PubMed: 17057713]

Procko E, O'Mara ML, Bennett WF, Tieleman DP, Gaudet R. The mechanism of ABC transporters: general lessons from structural and functional studies of an antigenic peptide transporter. FASEB J 2009;23:231–237.

Putnam CD, Hammel M, Hura GL, Tainer JA. X-ray solution scattering (SAXS) combined with crystallography and computation: defining accurate macromolecular structures, conformations and assemblies in solution. Q Rev Biophys 2007;40:191–285. [PubMed: 18078545]

Putnam CD, Clancy SB, Tsuruta H, Gonzalez S, Wetmur JG, Tainer JA. Structure and mechanism of the RuvB Holliday junction branch migration motor. J Mol Biol 2001;311:297–310. [PubMed: 11478862]

Rainbow RD, James M, Hudman D, Al Johi M, Singh H, Watson PJ, Ashmole I, Davies NW, Lodwick D, Norman RI. Proximal C-terminal domain of sulphonylurea receptor 2A interacts with pore-forming Kir6 subunits in K_{ATP} channels. Biochem J 2004;379:173–81. [PubMed: 14672537]

Rees DC, Johnson E, Lewinson O. ABC transporters: the power to change. Nat Rev Mol Cell Biol 2009;10:218–27. [PubMed: 19234479]

Reyes S, Park S, Johnson BD, Terzic A, Olson TM. K_{ATP} channel Kir6.2 E23K variant overrepresented in human heart failure is associated with impaired exercise stress response. Hum Genet. 2009 In Press.

Sattiraju S, Reyes S, Kane GC, Terzic A. K_{ATP} channel pharmacogenomics: from bench to bedside. Clin Pharmacol Ther 2008;83:354–7. [PubMed: 17957187]

Shi NQ, Ye B, Makielski JC. Function and distribution of the SUR isoforms and splice variants. J Mol Cell Cardiol 2005;39:51–60. [PubMed: 15978902]

Shyng S, Nichols CG. Octameric stoichiometry of the K_{ATP} channel complex. J Gen Physiol 1997;110:655–64. [PubMed: 9382894]

Solbach TF, Konig J, Fromm MF, Zolk O. ATP-binding cassette transporters in the heart. Trends Cardiovasc Med 2006;16:7–15. [PubMed: 16387624]

Svergun DI. Determinatiion of the regularization parameter in indirect-transform methods using perceptual criteria. J Appl Cryst 1992;25:495–503.

Svergun DI. Restoring low resolution structure of biological macromolecules from solution scattering using simulated annealing. Biophys J 1999;76:2879–86. [PubMed: 10354416]

Svergun DI, Koch MH. Advances in structure analysis using small-angle scattering in solution. Curr Opin Struct Biol 2002;12:654–60. [PubMed: 12464319]

Svergun DI, Barberato C, Koch MHJ. CRYSOL - a program to evaluate X-ray solution scattering of biological macromolecules from atomic cooridantes. J Appl Cryst 1995;28:768–773.

Svergun DI, Petoukhov MV, Koch MH. Determination of domain structure of proteins from X-ray solution scattering. Biophys J 2001;80:2946–53. [PubMed: 11371467]

Unneberg P, Merelo JJ, Chacon P, Moran F. SOMCD: method for evaluating protein secondary structure from UV circular dichroism spectra. Proteins 2001;42:460–70. [PubMed: 11170201]

Volkov VV, Svergun DI. Uniqueness of *ab initio* shape determination in small-angle scaterring. J Appl Cryst 2003;36:860–864.

Walker JE, Saraste M, Runswick MJ, Gay NJ. Distantly related sequences in the alpha- and beta-subunits of ATP synthase, myosin, kinases and other ATP-requiring enzymes and a common nucleotide binding fold. EMBO J 1982;1:945–51. [PubMed: 6329717]

Wheeler A, Wang C, Yang K, Fang K, Davis K, Styer AM, Mirshahi U, Moreau C, Revilloud J, Vivaudou M, Liu S, Mirshahi T, Chan KW. Coassembly of different sulfonylurea receptor subtypes extends the phenotypic diversity of ATP-sensitive potassium (K_{ATP}) channels. Mol Pharmacol 2008;74:1333–44. [PubMed: 18723823]

Yamada M, Kurachi Y. A functional role of the C-terminal 42 amino acids of SUR2A and SUR2B in the physiology and pharmacology of cardiovascular ATP-sensitive K^+ channels. J Mol Cell Cardiol 2005;39:1–6. [PubMed: 15978900]

Zingman LV, Alekseev AE, Hodgson-Zingman DM, Terzic A. ATP-sensitive potassium channels: metabolic sensing and cardioprotection. J Appl Physiol 2007;103:1888–93. [PubMed: 17641217]

Zingman LV, Alekseev AE, Bienengraeber M, Hodgson D, Karger AB, Dzeja PP, Terzic A. Signaling in channel/enzyme multimers: ATPase transitions in SUR module gate ATP-sensitive K^+ conductance. Neuron 2001;31:233–45. [PubMed: 11502255]

Zingman LV, Hodgson DM, Bienengraeber M, Karger AB, Kathmann EC, Alekseev AE, Terzic A. Tandem function of nucleotide binding domains confers competence to sulfonylurea receptor in gating ATP-sensitive K^+ channels. J Biol Chem 2002;277:14206–10. [PubMed: 11825892]

Zlatkovic J, Arrell DK, Kane GC, Miki T, Seino S, Terzic A. Proteomic profiling of K_{ATP} channel-deficient hypertensive heart maps risk for maladaptive cardiomyopathic outcome. Proteomics 2009;9:1314–25. [PubMed: 19253285]

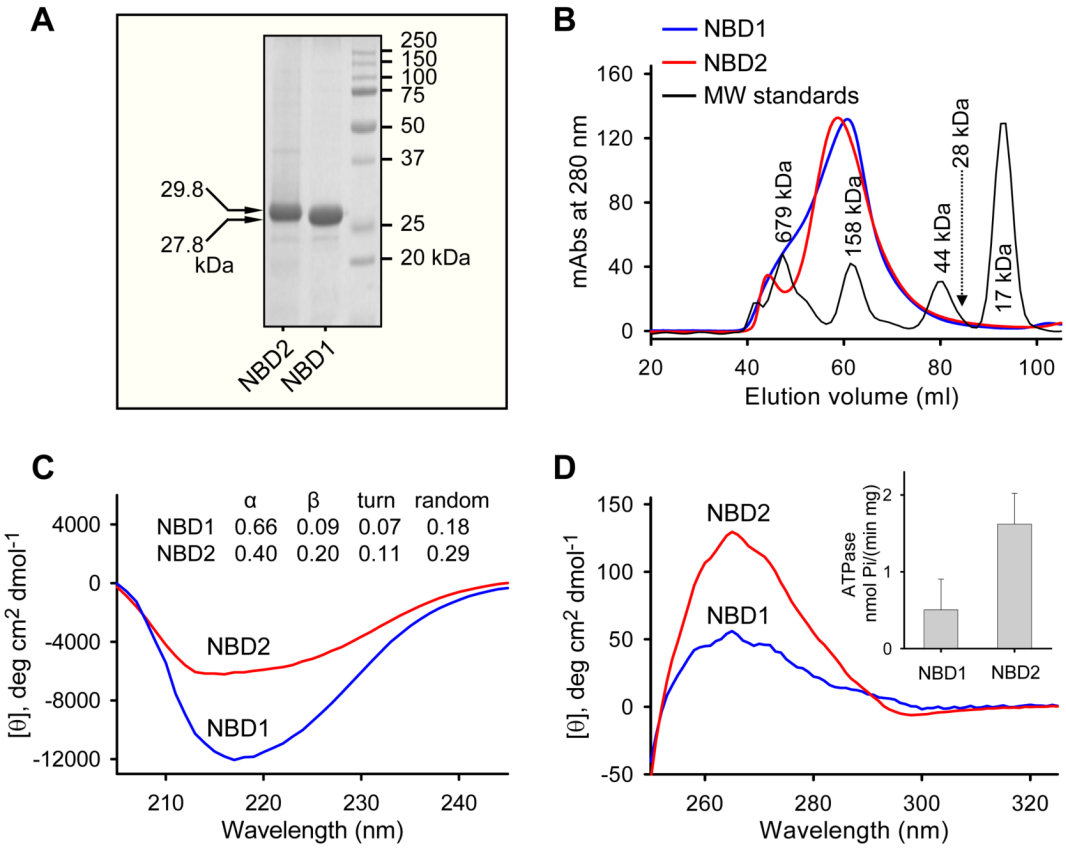

Figure 1.

Structural and functional integrity of refolded SUR2A NBD1/NBD2 proteins. Recombinant nucleotide binding domains, NBD1 and NBD2, were purified, refolded, and extracted from size exclusion chromatography. (A) Loaded at 7 μg/protein, Coomassie blue-stained NBD1 and NBD2 migrated at SDS-PAGE following expected molecular weights of 27.8 kDa and 29.8 kDa, respectively. (B) Superdex 200 gel filtration column elution of NBD1 and NBD2 demonstrated oligomeric profiles away from the monomeric 28 kDa protein. The far-UV (C) and near-UV (D) circular dichroism spectra revealed distinctive secondary and tertiary structures of NBD1 and NBD2. Inset: ATPase activity of NBD1 (0.51±0.37 nmol/mg/min, n=4) and NBD2 (1.62±0.41 nmol/mg/min, n=4) demonstrated functionality of refolded protein.

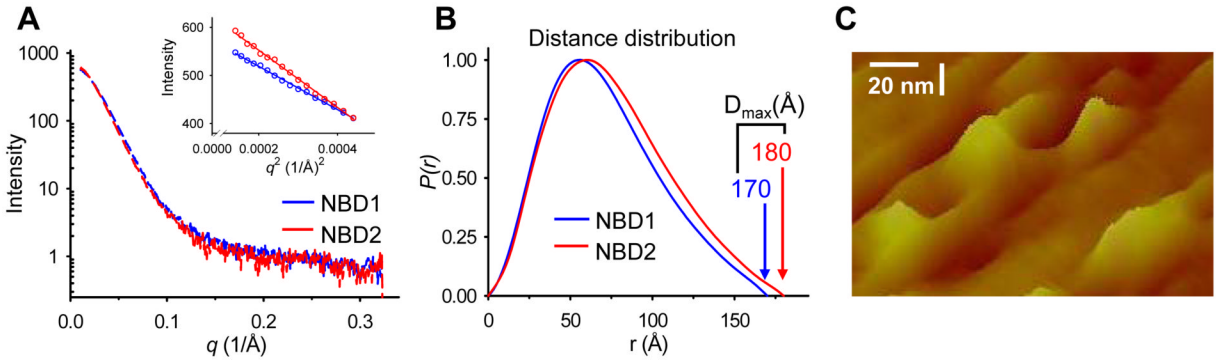

Figure 2.

Molecular outlines from interference-free NBD1 and NBD2. (A) Superimposed experimental SAXS curves from refolded NBD1 and NBD2. Inset: Guinier plots reflect homogeneous and monodisperse NBD1 and NBD2 in solution. (B) Distance distribution function, *(P(r))*, computed from experimental data and normalized to the maximum value of unity, demonstrated a maximum molecular dimension (D_{max}) at 170 and 180 Å for NBD1 and NBD2, respectively. (C) Atomic force microscopy in contact mode mapped the topography of NBD2 molecules (186±18 Å, n=8).

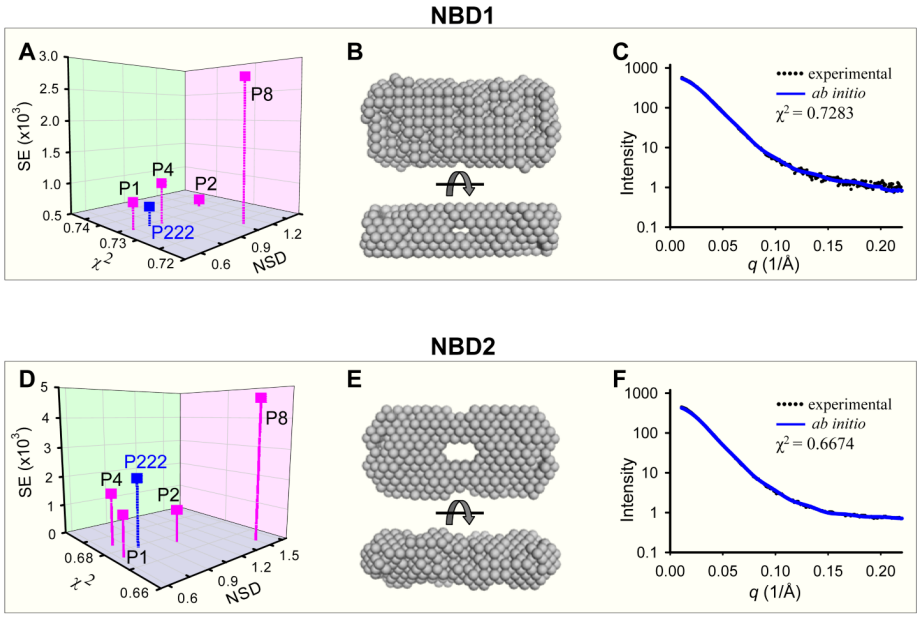

Figure 3.

Small angle X-ray scattering reconstruction of NBD1 and NBD2. *Ab initio* models of NBDs were determined from experimental SAXS data under different point-group symmetries using DAMMIN. The fits for NBD1 (A) and NBD2 (E) under different symmetry conditions are displayed as a function of normalized spatial discrepancy (NSD), discrepancy between the calculated and experimental SAXS curves (χ^2), and standard errors (SE) of χ^2. Sixteen independent runs were performed using P1, P2, P4, P8 and P222 symmetry. Ensemble average and respective fits for NBD1 (B and C) and NBD2 (E and F) based on P222 symmetry.

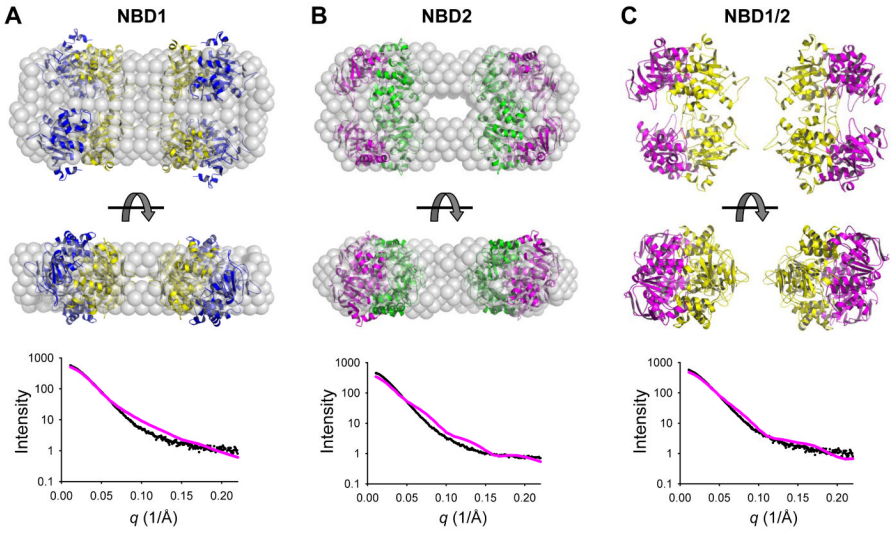

Figure 4.

Rigid body models of SUR2A NBD1(A), NBD2 (B) and NBD1/NBD2 (C) under P222 symmetry superimposed on *ab initio* envelopes. χ^2 values are 2.69 for NBD1, 4.09 for NBD2, and 2.86 for NBD1/NBD2. The inside and outside orientations of the octameric ring are denoted in yellow and blue for NBD1, and in green and purple for NBD2, respectively. In the NBD1/NBD2 structure, NBD1 is in yellow and NBD2 in purple. Scattering profiles (purple) from quaternary structure models of NBD1, NBD2 and NBD1/NBD2 were overlaid on experimental scattering curves (black).

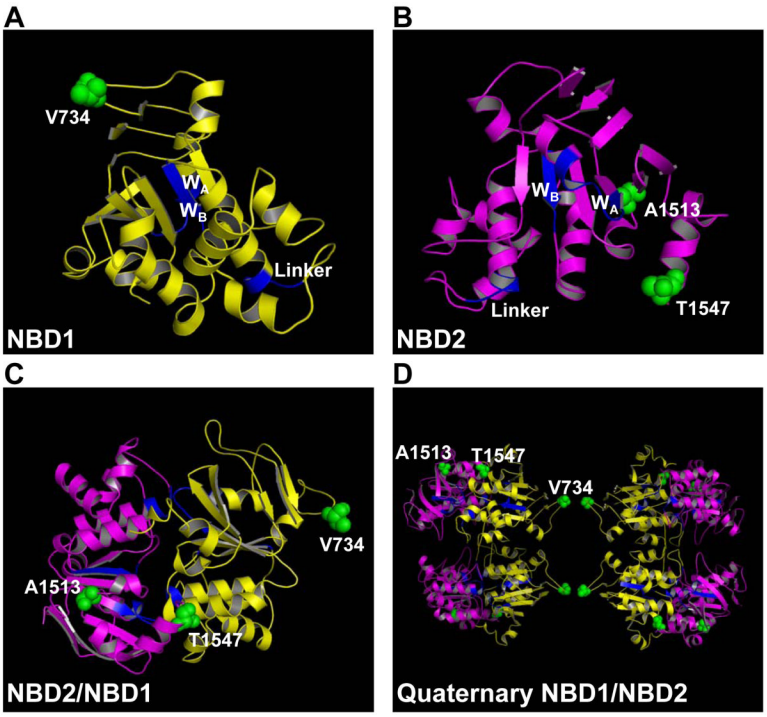

Figure 5.

Structure of NBDs incorporating pertinent pathogenic mutations found in human disease. (A) Homology structural model of NBD1 (A), NBD2 (B), NBD1/NBD2 (C), and SAXS resolved quaternary structure of NBD1/NBD2 (D) with mutated residues clustered at protein-protein interaction locales. NBD1 in yellow; NBD2 in purple; Walker A (W_A), Walker B (W_B), and linker motifs in blue; pathogenic human mutations in green.